AGU PUBLICATIONS

JGR

Journal of Geophysical Research: Atmospheres

RESEARCH ARTICLE
10.1002/2017JD027192

A Dynamical Explanation of the Topographically Bound Easterly Low-Level Jet Surrounding Antarctica

Scott R. Fulton[1], **Wayne H. Schubert**[2], **Zhengqing Chen**[1], **and Paul E. Ciesielski**[2]

[1]Department of Mathematics, Clarkson University, Potsdam, New York, USA, [2]Department of Atmospheric Science, Colorado State University, Fort Collins, Colorado, USA

Key Points:
- Balanced Antarctic circumpolar winds are modeled by inversion of potential vorticity
- The easterly low-level jet is due to topography and moderated by radiative cooling
- Dynamical connection of jet with katabatic winds is explained through the meridional circulation

Correspondence to:
S. R. Fulton,
fulton@clarkson.edu

Citation:
Fulton, S. R., Schubert, W. H., Chen, Z., & Ciesielski, P. E. (2017) A dynamical explanation of the topographically bound easterly low-level jet surrounding Antarctica. *Journal of Geophysical Research: Atmospheres*, *122*. https://doi.org/10.1002/2017JD027192

Received 25 MAY 2017
Accepted 2 NOV 2017
Accepted article online 7 NOV 2017

Abstract This study investigates the topographically bound easterly low-level jet surrounding Antarctica. This jet is modeled as a balanced flow that satisfies the potential vorticity invertibility principle, based on local linear balance in spherical coordinates and expressed in isentropic coordinates. In this way, this easterly low-level jet is shown to be the balanced flow associated with the topography of the Antarctic plateau, moderated by a shallow potential vorticity anomaly atop the plateau produced by radiative cooling. The dynamical connection of the jet with katabatic winds can be understood through the meridional circulation equation. Model results based on the simple theoretical arguments developed here are found to be consistent with high-resolution reanalysis data from the European Centre for Medium-Range Weather Forecasts for the 2008–2010 period.

Plain Language Summary This study investigates the persistent strong easterly wind (jet) that flows in the lower atmosphere along the eastern coastal region of Antarctica. It is shown that this low-level jet may be explained as a balanced flow—resulting from a dynamical balance between wind and pressure fields—associated with the cold, high Antarctic plateau. The explanation of this jet may lead to a better understanding of wind patterns over Antarctica and their relation to the topography of the continent.

1. Introduction

Two interesting aspects of the atmospheric flow in the Antarctic region are the katabatic winds, which flow down ice-covered slopes cooled by radiative processes, and the persistent easterly low-level jet (LLJ) surrounding the Antarctic plateau. Katabatic winds have received much attention in the literature; in contrast, the LLJ appears to have occasioned little mention. The primary aim of this paper is to explain this LLJ as a balanced flow induced by the topography of the polar plateau and moderated by the strong radiative cooling atop the plateau. A secondary aim is to identify the connections between this jet, the katabatic winds, and the radiative cooling that drives them.

One of the first maps of katabatic winds for the whole Antarctic continent was produced by Mather and Miller (1967) and later published by Mather (1969). This map of time-averaged surface streamlines, an adapted version of which is presented here as Figure 1, shows the katabatic flow toward the edge of the continent and its merger with the more geostrophic coastal easterlies, which occur over a nearly flat surface where the katabatic forcing disappears. A simple local theory of this boundary layer flow was developed by Ball (1960). As will be discussed in section 2, the solution of that slab boundary layer vector equation of motion shows that the resulting katabatic flow is not directly down the slope but is deflected to the left by the Coriolis force, a feature that is apparent in the observational data shown in Figure 1. A detailed analysis supporting the validity of this simple model of katabatic winds was provided by Parish and Bromwich (1987), who computed local model solutions on a 50 km × 50 km grid over the entire continent, using refined topographic data for computation of the local topographic slopes. The model results generally agree with the observations shown in Figure 1, but with considerable additional detail, especially in coastal valleys where there are "streamline confluence zones" at locations with intense katabatic winds (e.g., Cape Denison, the Amery Ice Shelf, and Terra Nova Bay). For further discussion of these topics and of Antarctic meteorology and climatology in general, the reader is referred to the comprehensive review given in the monograph by King and Turner (1997). More recently, Parish and Bromwich (2007) reexamined the mean near-surface airflow over Antarctica using archived data from the Antarctic Mesoscale Prediction System (AMPS), which is based on a polar-optimized

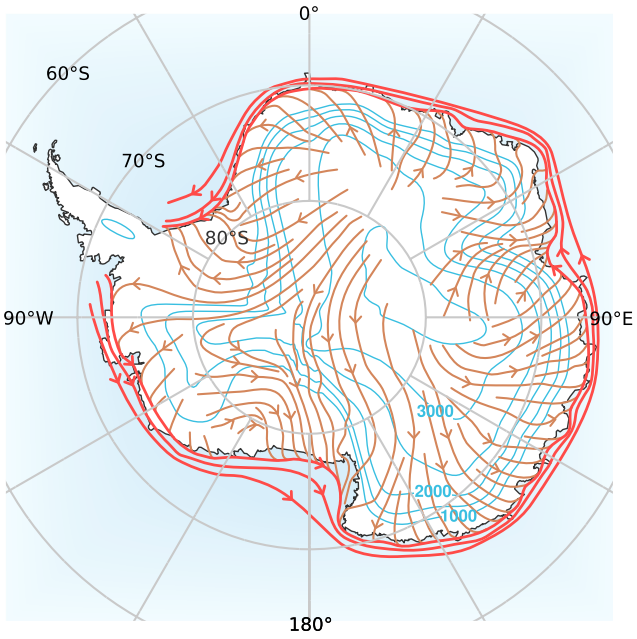

Figure 1. Topographic contours, labeled in meters, are shown by the blue lines. Time-averaged streamlines of the surface wind over the continent are shown by the brown lines. Streamlines of the coastal easterlies are shown in red. Note that the time-averaged surface flow is not directly down the local slope but is deflected to the left by the Coriolis force. Adapted from Figure 2 of Mather (1969).

mesoscale model. Their results show a close fit with those of Parish and Bromwich (1987). They argued that, although the drainage flows are very shallow, they are an important component of the mean meridional circulation and the large-scale tropospheric motions in the entire polar region.

While the coastal easterlies (indicated by the red streamlines in Figure 1) are primarily a low-level phenomenon, over the east coastal region a deeper easterly jet is evident in global reanalysis data sets. Here we use the high-resolution data set provided by the European Centre for Medium-Range Weather Forecasts from the "Year" of Tropical Convection (YOTC) reanalysis project (May 2008 to April 2010), as described by Waliser et al. (2012). The part of this data set used here has 6 h time resolution and 1.0° × 1.0° horizontal resolution (higher resolution is available), with 15 irregularly spaced vertical levels between 1,000 and 100 hPa. The circulation features of interest to this study are similar in both years of the YOTC analyses, so here results are presented for only one year. Figure 2 shows the mean winds and mean geopotential at 600 hPa in the Antarctic region, for the austral cold season 1 June 2009 to 31 August 2009 (denoted by JJA, left) and austral warm season 1 December 2009 to 28 February 2010 (denoted by DJF, right). A striking feature of both seasons is the anticyclonic flow that occurs over the elevated terrain of east Antarctica. While the cyclone over the Ross Ice Shelf (80°S, 165°W) is considerably stronger during the cold season, the structure and strength of the anticyclone is similar in the two seasons. Associated with this anticyclone is a significant easterly flow along the eastern coastal region; this flow is the easterly low-level jet, which is our main focus. To the best of our knowledge, this LLJ has not been singled out in previous studies nor has any dynamical explanation of it been proposed.

The vertical structure of this easterly LLJ is evident in Figure 3, which shows latitude-pressure cross sections averaged over the longitude sector 80–100°E for JJA (left column) and DJF (right column). This particular longitude band was chosen because of its zonal symmetry. Given the vertical resolution of the analysis, 15 levels are used in ocean regions and approximately 8 levels are used in regions of high topography. Figure 3 (top row) shows zonal winds in color. In this longitude band the easterly LLJ at the edge of the continent is clearly seen, with a peak easterly zonal velocity of 14.2 m s^{-1} in the cold season (JJA) and 11.3 m s^{-1} in the warm season (DJF). It should be noted that these cross sections are means over 3 months and 20° of longitude; for individual days and longitudes this easterly LLJ can be considerably stronger. Figure 3 (bottom row) shows corresponding cross sections of potential vorticity (PV). Of particular interest is the region of sharply enhanced PV immediately atop the polar plateau. This region, present in both seasons, is considerably stronger in the cold (JJA) season and may be attributed to the strong radiative cooling during the polar night. Together with the topography, this PV anomaly will figure prominently in our explanation of the easterly LLJ. Likewise, the enhanced PV in the upper-levels, associated with the increased static stability in the stratosphere, will also play a role.

The easterly LLJ should be present in simulations produced by numerical models of flow over Antarctica; for example, it is suggested in the AMPS results of Bromwich (2007, Figure 6b). However, to the best of our knowledge the only previous study to offer a PV interpretation of this flow is that of Kottmeier and Stuckenberg (1986). Following the arguments of Smith (1979), they developed a simple analytical model of the low-level circulation over Antarctica, using an *f*-plane argument based on the invertibility of quasi-geostrophic potential vorticity under the assumption that there are no potential vorticity anomalies in the interior of the fluid but that the lowermost isentropic surface has been bowed upward by the topography (an approximate quasi-geostrophic lower boundary condition). Although the model of Kottmeier and Stuckenberg has many approximations, it produces results that agree fairly well with observations that were available at that time, such as those found in Zwally et al. (1983). While they did not single it out, the easterly LLJ is evident in their Figures 4 and 6.

The primary goal of this paper is to offer a dynamical explanation of the easterly LLJ. Our analysis is in the same spirit as the quasi-geostrophic analysis given by Kottmeier and Stuckenberg but without many

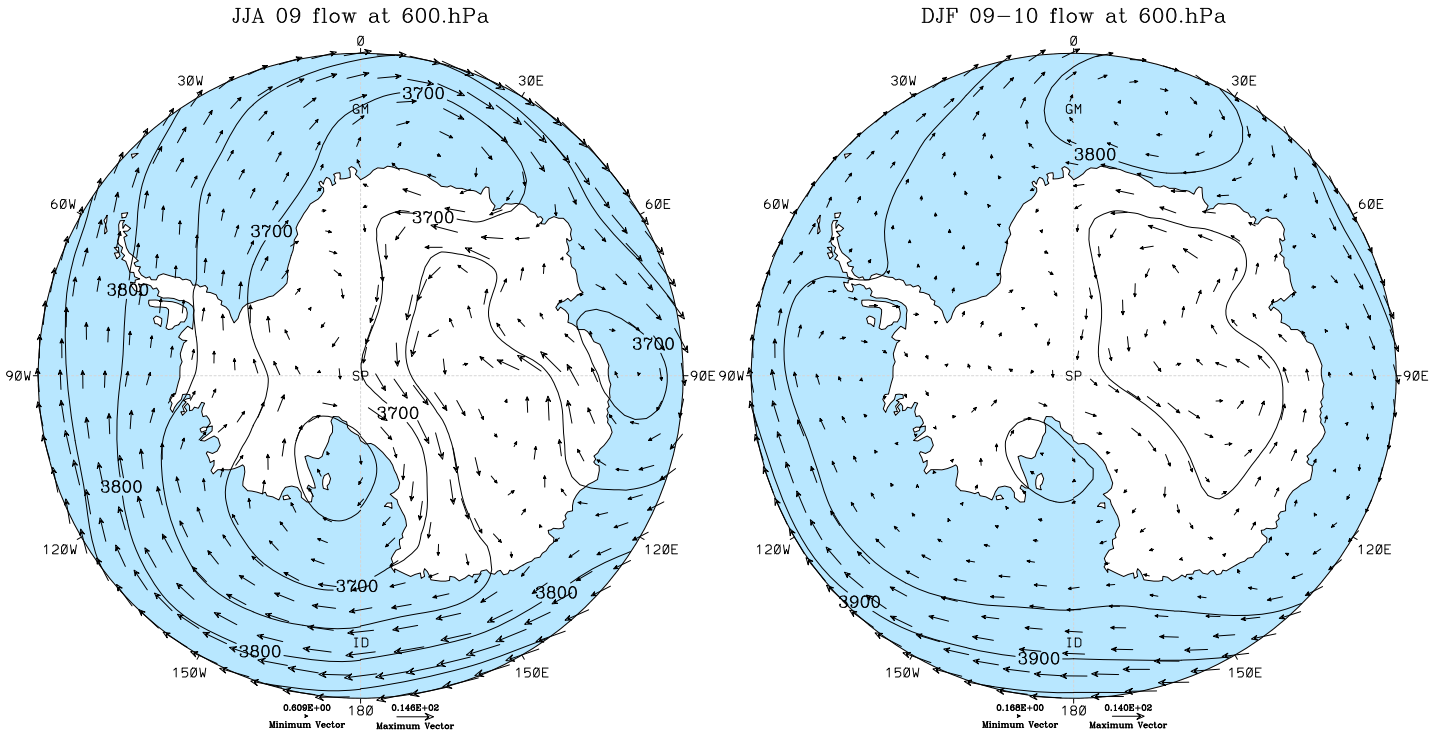

Figure 2. Mean wind and geopotential fields at 600 hPa from the YOTC analyses for the (left) 2009 cold season (JJA) and (right) 2009–2010 warm season (DJF). The outer edge of each map is at 60°S, with the Greenwich meridian at the top. The maximum wind speeds, indicated by the reference vectors at the bottom, are 14.6 m s^{-1} (JJA) and 14.0 m s^{-1} (DJF). The black contours are for geopotential with 50 m contour intervals.

of the approximations used in quasi-geostrophic theory. The approach is based on a zonally symmetric potential vorticity invertibility principle and includes vertical structure and more accurate versions of potential vorticity, dynamical balance, and the lower boundary condition. The theoretical basis for this approach was given by Eliassen (1980), who studied the topographically bound, balanced response of a rotating, stratified fluid to orography, and by Silvers and Schubert (2012), who applied these ideas to the low-level flows surrounding the Andes. Here we extend the latter analysis to the Antarctic region and thereby demonstrate that the Antarctic easterly LLJ can be interpreted as a balanced flow attributed—through the potential vorticity invertibility principle—primarily to the distribution of topography, to the fact that potential temperature varies little along this topography, and to the PV anomaly that resides just above the elevated ice sheet.

The paper is organized as follows. Section 2 reviews background for this problem, focusing on the Ball model that has been used in many previous studies of katabatic winds. Section 3 details our theoretical model based on the invertibility principle in isentropic coordinates. Section 4 presents results from this model, including a null case (which serves both as a test of the solution procedure and as a conceptual initial state), the balanced flow induced by an isentropic polar plateau, and the effects of lower-and-upper level PV anomalies and variations in top pressure and surface potential temperature. Section 5 considers the dynamical connections between radiative cooling, katabatic winds, and the easterly LLJ. Concluding remarks are given in section 6.

2. Background

Many previous studies of Antarctic winds have focused on low-level katabatic winds driven by radiative cooling and topography. In this section we briefly look at radiative cooling rates and then review the Ball model (which is central to the literature of such winds) in a particularly simple form. While this model is inadequate to explain the easterly LLJ, the radiative cooling and resulting katabatic flow that it produces are related to the meridional circulation that helps set up the conditions (distribution of potential vorticity and surface potential temperature) that give rise to that jet.

An important aspect of the boundary layer dynamics over the Antarctic and Greenland ice sheets during winter is the remarkable longwave radiative flux divergence that can occur within the lowest levels. This longwave

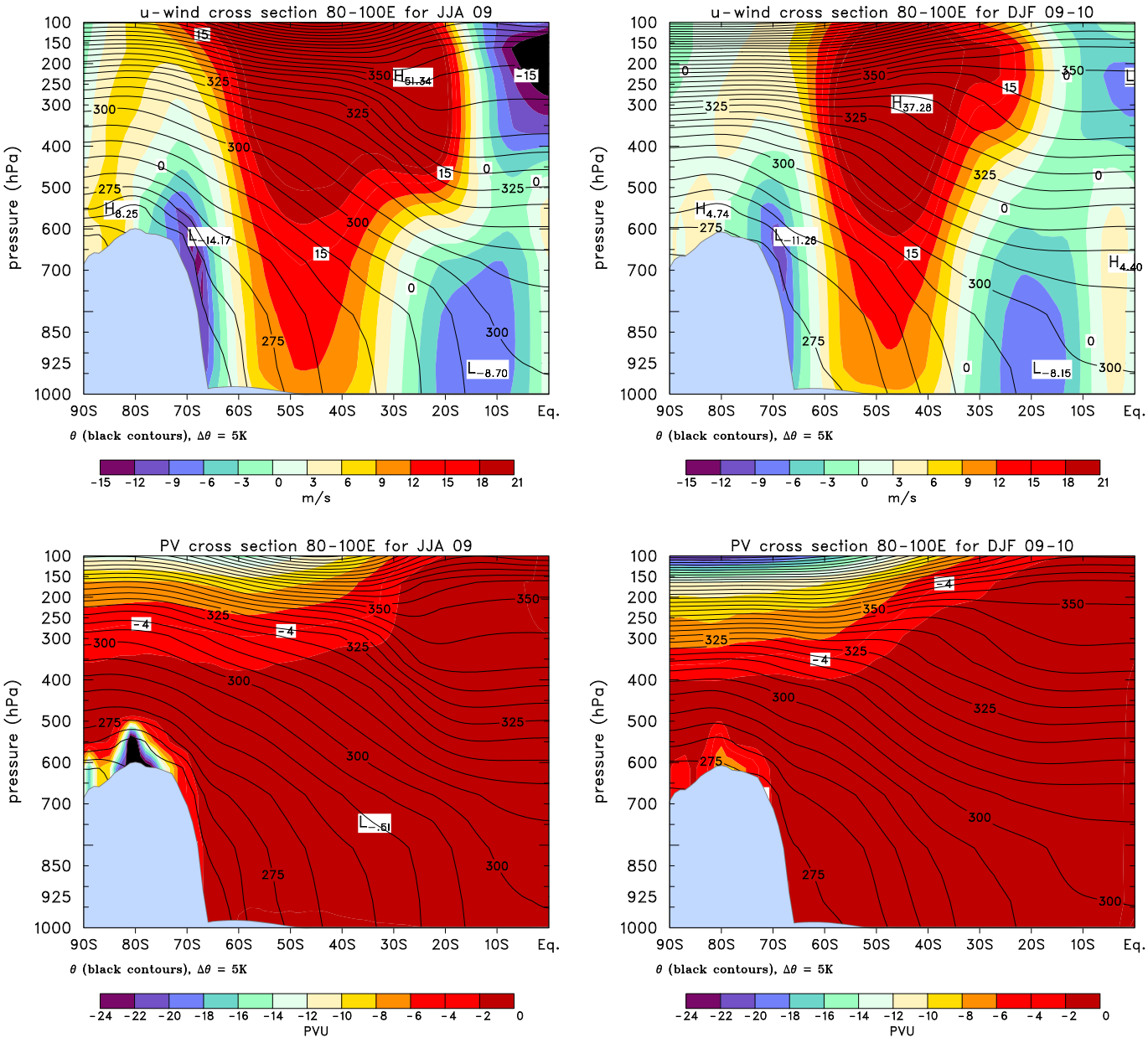

Figure 3. Mean latitude-pressure cross sections averaged over the longitude sector 80–100°E from the YOTC analyses for the (left column) cold season (JJA) and (right column) warm season (DJF). The top row shows zonal wind with magnitude given by the colorbar, which (for clarity) ends at 21 m s^{-1}, even though the upper-level westerlies are stronger. The bottom row shows PV with magnitude given by the colorbar, where one PV unit is defined as 10^{-6} m^2 s^{-1} K kg^{-1}. Black contours in each panel are isentropes at 5 K intervals.

radiative cooling leads to strong, wintertime low-level temperature inversions, as has been documented by Hudson and Brandt (2005), using data from radiosonde ascents and a 22 m tower at the South Pole station, and Hoch et al. (2007) using data from a 50 m tower erected on the Greenland ice sheet at an elevation of 3,203 m. In both of these regions low-level inversions of 10°C in the lowest 50 m are typical for wintertime conditions. The measurements of Hoch et al. (2007) are unique in that infrared radiometers were used to measure downward and upward longwave fluxes at 2 m and 48 m above the ice surface for the period from June 2001 to July 2002. This makes possible the computation of the divergence of the longwave flux and hence longwave cooling rates over an annual cycle. The summer situation, which is complicated by the presence of fog, low clouds, and a significant diurnal cycle, exhibits a daily-mean net longwave cooling rate in the lowest layers of 2°C/d. The winter situation is simpler, as there is no diurnal cycle and a quasi-steady, low-level, temperature inversion is established. While in a typical winter situation over Greenland, the downward longwave flux

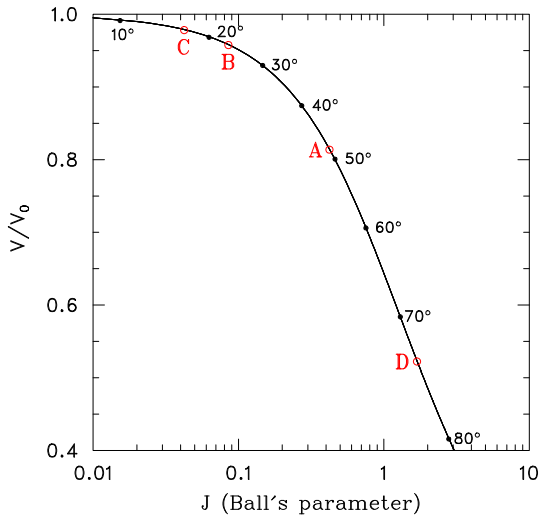

Figure 4. Dimensionless wind speed V/V_0 as a function of the dimensionless parameter J, as determined by (3). The points along the curve give the wind direction β, as determined by (4). Note that small values of J correspond to strong forcing, while large values of J correspond to weak forcing.

is generally small, resulting in negligible heating or cooling rates, this is more than offset by the divergence of the upward longwave flux, which (by itself) would cause a radiative cooling of 10–30°C/d. Therefore, the mean wintertime net longwave radiative cooling is 11°C/d in the lowest 50 m (Hoch et al., 2007). There is also evidence that larger cooling rates are associated with stronger inversions, so there may be a positive feedback mechanism for the establishment of strong inversions. Thus, over Greenland and presumably also over Antarctica, longwave radiative cooling during winter is capable of establishing a strong low-level temperature inversion in a day or two. Subsequently, this radiative cooling is capable of maintaining a quasi-steady inversion in spite of the fact that vertical and horizontal advective processes in the thermodynamic equation may tend to destroy the inversion.

A strong temperature inversion near the surface takes on crucial dynamical importance when the surface topography is sufficiently sloped that katabatic winds develop. The dynamics of such flows were illuminated by Ball (1960), who proposed a steady state, constant depth, slab boundary layer model for flow over sloping topography and under a temperature inversion. In order to understand the successes and limitations of the Ball model, consider the coordinate-independent vector form given by

$$f\mathbf{k}\times\mathbf{u}+\frac{kV}{h}\mathbf{u}=\mathbf{F}, \tag{1}$$

where the specified boundary layer forcing is given by

$$\mathbf{F}=-\frac{1}{\rho}\nabla p-\frac{\Delta T}{\bar{T}}\nabla\Phi_S, \tag{2}$$

with $\mathbf{u}$ denoting the horizontal vector velocity, $V=|\mathbf{u}|$ the wind speed, f the Coriolis parameter, $\mathbf{k}$ the vertical unit vector, k the dimensionless frictional constant, h the constant boundary layer depth, ρ the constant boundary layer density, p the specified pressure field, $\bar{T}$ the constant reference temperature, ΔT the inversion strength, Φ_S the specified surface geopotential, and ∇ the horizontal gradient operator. The first term on the right-hand side of (2) represents the pressure gradient force imposed on the boundary layer by the overlying fluid, while the final term represents the sloped inversion pressure gradient force, which is proportional to the product of the inversion strength and the topographic slope. In the absence of the sloped inversion pressure gradient force (e.g., in the case $\Phi_S=0$), the Ball model (1) reduces to the classical, steady state, slab Ekman layer model, which assumes a balance between the Coriolis force, the frictional force, and the imposed pressure gradient force. Thus, the Ball model is a generalization of classic Ekman theory to include the effects of the sloped inversion pressure gradient force. Equation (1) is a "local" relation in the sense that $\mathbf{u}$ at a particular point depends only on the value of $\mathbf{F}$ at that point.

The Ball model can be solved analytically (see Appendix A) for the wind speed

$$V=V_0\left[\left(J^2+1\right)^{1/2}-J\right]^{1/2} \tag{3}$$

and direction angle

$$\beta=\cos^{-1}\left(\frac{V^2}{V_0^2}\right) \tag{4}$$

relative to $\mathbf{F}$, where $V_0=(hk^{-1}\,|\mathbf{F}|)^{1/2}$ and $J=(f^2h)(2k\,|\mathbf{F}|)^{-1}$. A physical interpretation of V_0 can be obtained by noting that, in the special case $f=0$, "Ball's parameter" J vanishes and $V=V_0$, a result that also follows by taking the magnitude of (1). Thus, V_0 can be interpreted as the wind speed that would occur on a nonrotating Earth. Figure 4 shows V/V_0 as a function of J, with corresponding values of β at 10° intervals indicated by the dots.

To obtain an appreciation of the typical values of the quantities involved in the Ball model as applied to the Antarctic, we have prepared Table 1, whose four rows correspond, respectively, to the points A, B, C, and D in Figure 4, with point A near the relatively flat, high interior (slope 1/1,000 and $\Delta T=24$°C), point B on the

Table 1
Solutions of the Ball Model for Four Typical Points: A (High Interior Point With Very Gentle Slope); B (Intermediate Point With Gentle Slope); C (Intermediate Point With Steep Slope); D (Coastal Point With Very Gentle Slope)

Point	$\Delta T/\bar{T}$	$g^{-1}\nabla\Phi_S$	V_0 (m s^{-1})	J	V/V_0	V (m s^{-1})	β (deg)
A (interior)	24/240	1/1,000	6.26	0.42084	0.81493	5.10	48.4
B (intermediate)	12/240	1/100	14.00	0.08417	0.95884	13.42	23.2
C (intermediate)	12/240	1/50	19.80	0.04208	0.97918	19.39	16.5
D (coastal)	6/240	1/1,000	3.13	1.68334	0.52405	1.64	74.1

Note. The chosen constants are $g = 9.8$ m s^{-2}, $f = 1.436 \times 10^{-4}$ s^{-1}, $k = 5 \times 10^{-3}$, and $h = 200$ m.

more strongly sloped terrain away from the interior (slope 1/100 and $\Delta T = 12°$C), point C on the even more strongly sloped terrain (slope 1/50 and $\Delta T = 12°$C), and point D near the edge of the continent (slope 1/1,000 and $\Delta T = 6°$C). The chosen values of ΔT are taken from the Antarctic temperature inversion map of Phillpot and Zillman (1970). Point C has the strongest forcing, so it has the smallest value of J and the largest value of V_0. For cases in which $\nabla p = 0$, the forcing (2) is entirely due to the sloped inversion effect, so that the vector **F** points directly downslope. Then, for the strong flow case C, the wind direction is only 16.5° to the left of the downslope direction, while for the weak flow coastal case D, the wind direction is 74.1° to the left of the downslope direction.

The results of the Ball model are consistent with the observations of a low-level easterly flow surrounding Antarctica (e.g., Figure 1). However, since it is based on a local force balance in a slab boundary layer, it cannot explain the observed horizontal and vertical structure of the easterly LLJ. Indeed, as pointed out by Parish and Bromwich (2007), deep Antarctic flow that appears to be bound to the topography is not merely a katabatic phenomenon. In the following section we shall develop an alternative theoretical model based on PV dynamics (in particular, on the nonlocal PV invertibility principle), which can explain the LLJ. After presenting results from that model (section 4), we will then discuss how that jet is related to the radiative cooling and the resulting meridional circulation represented by the Ball model (section 5).

3. Theoretical Model

The analysis begins by considering hydrostatic motions of a compressible stratified fluid on the sphere, using the longitude λ and the latitude ϕ as the horizontal coordinates. The potential temperature θ is used as the vertical coordinate, in order to obtain a simple form of the invertibility relation. The potential vorticity is

$$P = \frac{g(f+\zeta)}{\sigma}, \tag{5}$$

where g is the acceleration of gravity, $f = 2\Omega \sin\phi$ the Coriolis parameter (with Ω the rotation rate of the Earth), ζ the isentropic relative vorticity, and $\sigma = -\partial p/\partial\theta$ the pseudodensity, with p the pressure. Using the ideal gas law to express the density as $\rho = p/(\mathrm{RT}) = c_p p/(R\theta\Pi)$, where $\Pi = c_p(p/p_0)^{R/c_p}$ (with p_0 denoting the constant reference pressure, R the gas constant, and c_p the specific heat at constant pressure), it is easily shown that $\theta\rho(d\Pi/dp) = 1$. This allows (5) to be written in the form

$$\frac{g}{\theta\rho P}(f+\zeta) + \frac{\partial\Pi}{\partial\theta} = 0. \tag{6}$$

The zonal and meridional components of the nondivergent part of the flow, denoted by u_ψ and v_ψ, respectively, are related to the stream function ψ by

$$(u_\psi, v_\psi) = \left(-\frac{\partial\psi}{a\partial\phi}, \frac{\partial\psi}{a\cos\phi\partial\lambda}\right) \tag{7}$$

(where a is the radius of the Earth), so that the isentropic relative vorticity can be expressed as

$$\begin{aligned}\zeta &= \frac{\partial v_\psi}{a\cos\phi\,\partial\lambda} - \frac{\partial(u_\psi\cos\phi)}{a\cos\phi\,\partial\phi} \\ &= \frac{\partial^2\psi}{a^2\cos^2\phi\,\partial\lambda^2} + \frac{\partial}{a\cos\phi\,\partial\phi}\left(\cos\phi\frac{\partial\psi}{a\partial\phi}\right) = \nabla^2\psi.\end{aligned} \tag{8}$$

Using this result and the hydrostatic relation $\Pi = \partial M/\partial\theta$, where $M = \theta\Pi + \Phi$ is the Montgomery potential and Φ is the geopotential, we can rewrite (6) as

$$\frac{g}{\theta\rho P}\left(f + \nabla^2\psi\right) + \frac{\partial^2 M}{\partial\theta^2} = 0. \tag{9}$$

When isentropic surfaces intersect the Earth's surface, they can be considered to run along the Earth's surface with a pressure equal to the surface pressure, thereby forming a massless layer with infinite potential vorticity (i.e., $\sigma \to 0$ and $P \to \infty$). We define $\theta_S(\lambda, \phi)$ as the actual value of potential temperature on the Earth's surface and work on a domain in θ bounded by constants θ_B and θ_T satisfying $\theta_B \le \theta_S(\lambda, \phi) < \theta_T$ over the horizontal domain of interest. Then the region $\theta_B \le \theta < \theta_S(\lambda, \phi)$ is the massless layer and the region $\theta_S(\lambda, \phi) < \theta \le \theta_T$ is the atmosphere. We use the subscript S to denote surface values (i.e., values at $\theta = \theta_S$) of other fields. Then in the massless layer, $\sigma = 0$, $p = p_S$, $\Pi = \Pi_S$, $\Phi = \Phi_S$, and $M = \theta\Pi_S + \Phi_S$. All mass variables other than σ are continuous at θ_S. The usual relations between the mass variables hold in the massless layer; a careful analysis (Fulton & Schubert, 1991, Appendix) shows that the hydrostatic equation also holds at $\theta = \theta_S$. While (9) holds in the atmosphere ($\theta > \theta_S$), it reduces to

$$\frac{\partial^2 M}{\partial\theta^2} = 0 \tag{10}$$

in the massless layer ($\theta < \theta_S$) since $P \to \infty$ there.

Equations (9) and (10) relate the potential vorticity field P, the wind field ψ, and the mass field M. To convert these into an invertibility relation, we now introduce a balance condition between ψ and M. The relation between the wind field and the mass field is assumed to be local linear balance, which is discussed in several different contexts by Kuo (1959), Charney and Stern (1962), and Schubert, Taft, et al. (2009). The isentropic coordinate version of local linear balance is

$$M(\lambda, \phi, \theta) = \tilde{M}(\theta) + f\,\psi(\lambda, \phi, \theta), \tag{11}$$

where $\tilde{M}(\theta)$ is a specified reference state, corresponding to pressure $\tilde{p}(\theta)$, density $\tilde{\rho}(\theta)$, and pseudodensity $\tilde{\sigma}(\theta) = -d\tilde{p}/d\theta$ satisfying

$$\frac{d\tilde{M}}{d\theta} = \tilde{\Pi} = c_p\left(\frac{\tilde{p}}{p_0}\right)^{R/c_p}, \quad \tilde{\rho} = \frac{p_0}{R\theta}\left(\frac{\tilde{\Pi}}{c_p}\right)^{c_v/R}, \tag{12}$$

with $\tilde{M}(\theta_B) = c_p\theta_B$, and with $c_v = c_p - R$ denoting the specific heat at constant volume. Using the balance condition (11) in (9) and (10), we can write the invertibility relation in the form

$$\alpha\nabla^2\psi + f\frac{\partial^2\psi}{\partial\theta^2} = \frac{\tilde{\sigma}}{\theta\tilde{\rho}} - \alpha f, \tag{13}$$

where

$$\alpha = \begin{cases} \dfrac{g}{\theta\rho P}, & \theta_S < \theta < \theta_T \quad \text{[atmosphere]}, \\ 0, & \theta_B < \theta < \theta_S \quad \text{[massless layer]}. \end{cases} \tag{14}$$

Since α depends on ρ through (14) and ρ depends on ψ through

$$\rho = \frac{p_0}{R\theta}\left(\frac{\Pi}{c_p}\right)^{c_v/R}, \quad \Pi = \tilde{\Pi} + f\frac{\partial\psi}{\partial\theta}, \tag{15}$$

equation (13) is quasilinear. It is elliptic if α and f have the same sign, that is, if $P < 0$ in the Southern Hemisphere and $P > 0$ in the Northern Hemisphere. Experience has shown (Schubert & Masarik, 2006; Schubert, Silvers, et al., 2009) that we can regard (13) as an invertibility principle that is valid over the entire sphere.

We wish to solve the invertibility relation on the region $\phi_S < \phi < \phi_N$, where $\phi_S = -\pi/2$ is the South Pole and ϕ_N is a fixed latitude. For the lateral boundary condition we specify M as in the reference state (20) below, except with θ_B replaced by $\theta_S(\phi_N)$, and compute Dirichlet values of ψ accordingly. For the upper boundary condition we specify the pressure $p_T(\lambda, \phi) = p(\lambda, \phi, \theta_T)$ on the upper isentropic surface $\theta = \theta_T$, leading to

$$f\left(\frac{\partial\psi}{\partial\theta}\right) = \Pi_T - \tilde{\Pi}_T \quad \text{at } \theta = \theta_T, \tag{16}$$

where $\Pi_T(\lambda, \phi)$ corresponds to the specified top pressure. For the lower boundary condition we apply the general relation $M - \theta(\partial M/\partial\theta) = \Phi$ at $\theta = \theta_B$, resulting in

$$f\left(\psi - \theta\frac{\partial\psi}{\partial\theta}\right) = \Phi_S \quad \text{at } \theta = \theta_B, \tag{17}$$

where the surface geopotential $\Phi_S(\lambda, \phi)$ is specified, giving the topography.

In summary, the invertibility problem consists of (13)–(17). To solve the problem for ψ, we must specify the constants θ_B, θ_T, ϕ_N, the reference state, the potential vorticity P on the domain, and the boundary data θ_S, Φ_S, and p_T.

For simplicity we now restrict our attention to the two-dimensional version of (13)–(17) under the assumption that all fields are independent of longitude. In this case the Laplacian (8) reduces to

$$\nabla^2\psi = \frac{1}{\cos\phi}\frac{\partial}{a\partial\phi}\left(\cos\phi\frac{\partial\psi}{a\partial\phi}\right). \tag{18}$$

This operator is singular at the poles $\phi = \pm\pi/2$; since by symmetry $\partial\psi/\partial\phi = 0$ there, we can use L'Hôpital's Rule to replace (18) by the limiting form

$$\nabla^2\psi = \frac{2}{a^2}\frac{\partial^2\psi}{\partial\phi^2} \qquad \text{at } \phi = \pm\frac{\pi}{2}. \tag{19}$$

The numerical method used to solve this problem is described in Appendix B.

For the results presented below we will take the northern boundary to be $\phi_N = -20°$, and unless otherwise noted we will take the top pressure p_T to be constant. The reference state is taken to be

$$\tilde{M}(\theta) = \Pi_B\theta - \frac{(\Pi_B - \Pi_T)}{2(\theta_T - \theta_B)}\left(\theta - \theta_B\right)^2, \tag{20}$$

which gives Π linear in θ and buoyancy frequency inversely proportional to θ. This is the same reference state as used by Silvers and Schubert (2012), and is shown in their Figure 5. Unless otherwise specified, the constants are given by $\theta_B = 260$ K and $\theta_T = 370$ K, with Π_B and Π_T based on $p_B = p_0 = 1,000$ hPa and $p_T = 100$ hPa.

4. Results

This section presents results from the theoretical model described above, including a null case (which serves both as a test of the solution procedure and as a conceptual initial state), the balanced flow induced by an isentropic polar plateau, and the effects of surface potential temperature and top pressure variations. The zonally symmetric model results presented here are intended to represent fields over Eastern Antarctica as depicted in Figure 3.

4.1. Null Case

A useful test of the solution procedure is as follows. If we specify $P = \tilde{P} = gf/\tilde{\sigma}$, then $\psi = 0$ solves (13) in the atmosphere. If $\psi = 0$ also satisfies the boundary conditions, then there is no flow; this occurs when θ_S and Φ_S are specified such that

$$\tilde{\Phi}(\theta_S(\phi)) = \Phi_S(\phi). \tag{21}$$

Combined with the reference state (20), (21) allows us to compute $\theta_S(\phi)$ from any specified topography $\Phi_S(\phi)$. Figure 5 shows the solution of this "null case," where the topography is given by (22) below. As expected, the mass field is horizontally homogeneous and the zonal wind is essentially zero outside the massless region. The anticyclone in the massless region of Figure 5 (bottom) has no physical significance and, in fact, is not present in the (ϕ, p) space shown in Figure 5 (top). However, it is important to keep in mind that, in order to produce Figure 5, the PV invertibility problem has been solved in (ϕ, θ) space in the entire domain shown in Figure 5 (bottom), including points in the massless region at the lower left. The calculations performed in this massless region can be considered the overhead cost for the convenience of working in a computational domain that has the isentropic surface $\theta = 260$ K as the lower boundary. It is also important to note that,

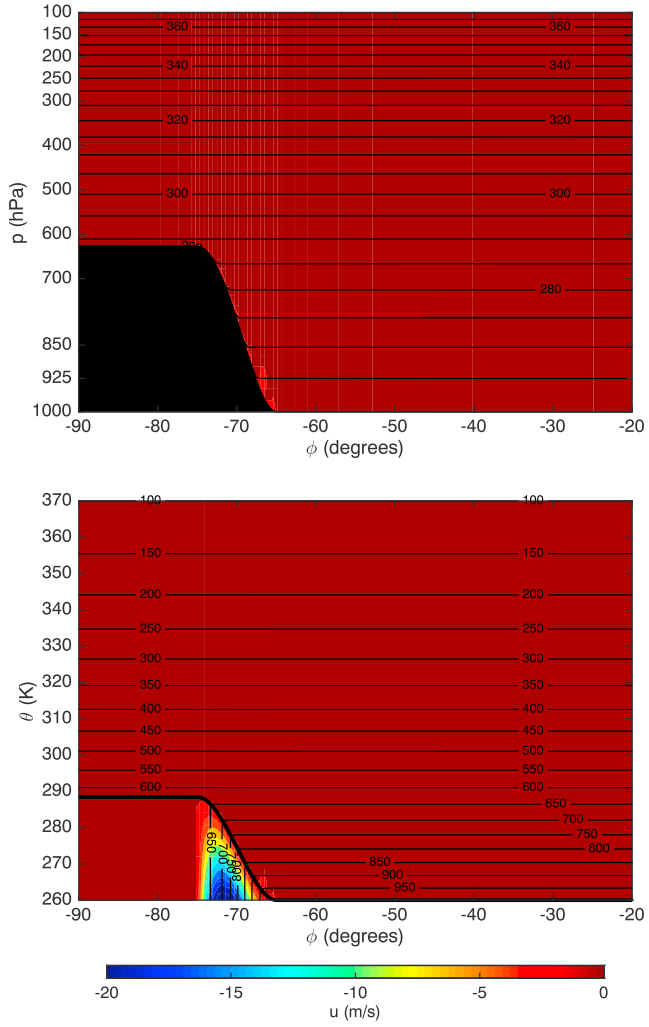

Figure 5. Zonal wind field (shading, 2 m s^{-1} intervals) for the null case described in the text. The massless layer is indicated in (top) (ϕ, p) space by the black region along the lower boundary and in (bottom) (ϕ, θ) space by the thick black line corresponding to $\theta_S(\phi)$. Black lines are isentropes (top, spacing 5 K) and isobars (bottom, spacing 50 hPa).

while there is infinite PV in the massless region, it does not induce any zonal flow the in atmosphere (i.e., outside the massless region) because the specified functions $\Phi_S(\phi)$, $\theta_S(\phi)$, and $\tilde{\Phi}_S(\theta)$ satisfy (21).

While the null case shown in Figure 5 is obviously quite different than the observations shown in Figure 3, we may use it as a conceptual "initial state" to understand the development of the easterly low-level jet as follows. Starting with the null case, consider how the atmosphere would respond to radiative cooling of the polar plateau. With $\dot{\theta} < 0$ on the top and slope of the plateau, isentropes would be forced locally upward. If the cooling were slow, a balanced secondary (meridional) circulation would develop. If the cooling were fast, the response would be more complicated and involve propagating gravity-inertia waves superimposed on the balanced secondary circulation. Thus, for simplicity, suppose the cooling is slow.

Since the concentrated radiative cooling at the surface moves mass downward across isentropic surfaces, in the (ϕ, p) space view of Figure 5 (top) the θ surfaces creep upward relative to the plateau, so the $\theta = 288$ K surface, which initially was at the top of the plateau, is pushed upward into the free atmosphere above the plateau. In the (ϕ, θ) space view of Figure 5 (bottom), the top of the massless layer shifts downward from $\theta = 288$ K to $\theta = 287$ K, say. In other words, the radiative cooling is acting to remove the massless layer. After a sufficient time, isentropes will have crept upward along the slope until a nearly isentropic barrier exists, that is, the massless layer has almost completely disappeared. At the same time, the radiative cooling is producing a PV anomaly in the fluid just above the crest. In the second order partial differential equation (13), the spatially varying factor α, defined in (14), is continually changing because of the slow time variation of both $P(\phi, \theta)$ and $\theta_S(\phi)$. Since both $P(\phi, \theta)$ and $\theta_S(\phi)$ are part of the specified data for the invertibility problem, they both influence the resulting balanced wind and mass fields, that is, they both influence the strength and structure of the easterly LLJ. In the remainder of this section we show how the anomaly in $P(\phi, \theta)$ can moderate the strength of the easterly jet attributed primarily to the topography, and that the variation of $\theta_S(\phi)$ plays a relatively small role.

4.2. Isentropic Polar Plateau

The YOTC analyses shown in Figure 3 indicate that the Antarctic plateau is to a first approximation an isentropic obstacle: the 265 K isentrope nearly follows the Antarctic topography in the cold season (JJA), while the 275 K isentrope nearly follows the topography in the warm season (DJF). This is consistent with the conceptual arguments above. Therefore, we now compute the balanced flow associated with a polar plateau with an isentropic lower boundary, that is, $\theta_S(\phi) = \theta_B$, so there is no massless layer. We specify geopotential at the lower boundary to vary from gH at ϕ_a to 0 at ϕ_b via

$$\Phi_S(\phi) = gH \begin{cases} 1, & \phi_S \le \phi \le \phi_a, \\ S_\Phi\left(\dfrac{\phi - \phi_a}{\phi_b - \phi_a}\right), & \phi_a \le \phi \le \phi_b, \\ 0, & \phi_b \le \phi \le \phi_N, \end{cases} \tag{22}$$

where $S_\Phi(s) = 1 - 3s^2 + 2s^3$ is a cubic Hermite function giving a smooth transition from 1 at $s = 0$ to 0 at $s = 1$. This specification of $\Phi_S(\phi)$ is designed to give a rough approximation to the actual topography of Antarctica at longitude 90°E. For the calculations presented here we use $H = 3,500$ m, $\phi_a = -75°$, and $\phi_b = -65°$ unless otherwise noted.

For the potential vorticity, we first define a "background" potential vorticity $\bar{P}(\phi, \theta) = gf(\phi)/\bar{\sigma}(\phi, \theta)$ with $\bar{\sigma}$ computed as in the reference state (20), except with θ_B replaced by $\theta_S(\phi)$ and Π_T computed from $p_T(\phi)$. This definition anticipates cases with variable $\theta_S(\phi)$ and $p_T(\phi)$ below; for the isentropic case here, $\bar{P} = \tilde{P}$.

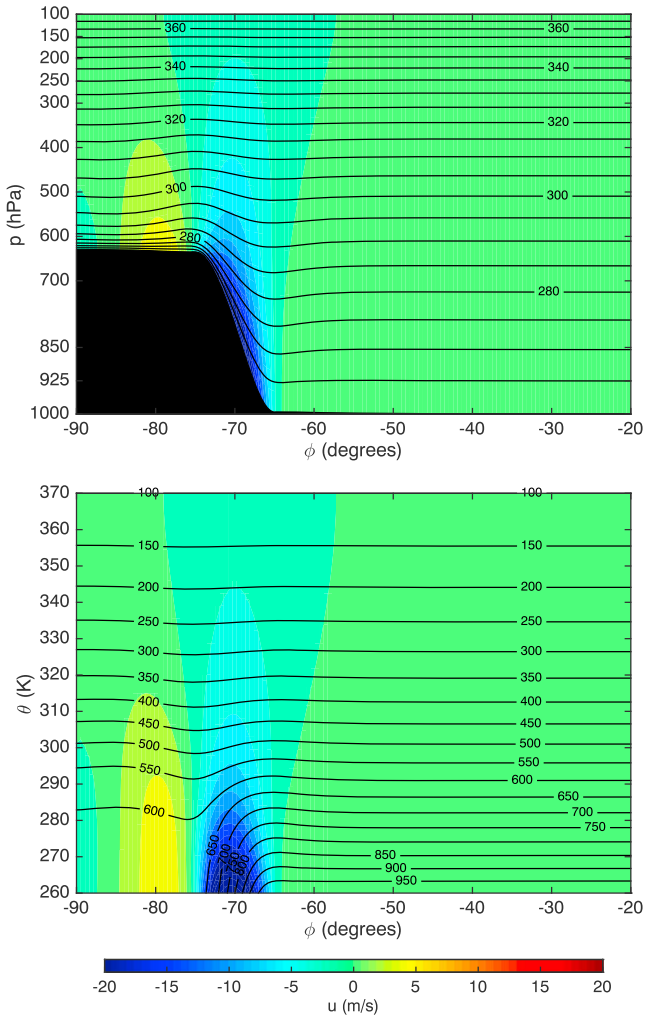

Figure 6. Zonal wind field (shading, 2 m s^{-1} intervals) for the case of an isentropic polar plateau. Isentropes in (top) (ϕ, p) space and (bottom) isobars in (ϕ, θ) space are as in Figure 5. The maximum easterly wind is 28.3 m s^{-1}, with a maximum westerly wind of 5.3 m s^{-1} above the plateau.

This background PV varies smoothly from about −0.3 PV units at the lower surface at the northern boundary to about −4.8 PV units at the top boundary at the South Pole, growing more negative with increasing θ (due to the variation of $\bar{\sigma}$) and with decreasing ϕ (due to the variation of f). With this PV distribution the solution of the invertibility problem (not shown) exhibits an easterly jet along the slope of the plateau as expected; however, the wind speeds are unrealistically high (about 45 m s^{-1}), as are the pressures in the area of the plateau (about 800 hPa at the pole). This is remedied by including a region of enhanced PV on top of the plateau as present in the YOTC analyses shown in Figure 3 to account for the strong radiative cooling over the polar plateau. Using Figure 3 (JJA of 2009) as a guide, this is specified as a Gaussian function with e-folding width 10° in latitude and 20 K in θ, centered at $\phi = -85°$ and $\theta = \theta_B$, and amplitude −18.6 PV units (20 times the background PV there, giving a minimum value of −19.5 PV units, in line with the YOTC data). This specification of background PV and low-level PV anomaly is used for all subsequent results unless otherwise specified; small changes in the details of the anomaly (size, location, and strength) make relatively little difference in the solutions obtained.

Figure 6 shows the zonal wind field that results from this isentropic polar plateau. The easterly low-level jet is clearly captured in this solution, with input based only on the topography of the plateau and the region of enhanced PV above it. The effect of the PV anomaly is to moderate the strength of the jet as compared to the effect of topography alone. The jet is still stronger than in the YOTC analyses of Figure 3, but that is due in part to the lack of surface friction in the model. The weaker westerly flow on the top of the plateau is in qualitative agreement with the data.

In Figure 6 the lower boundary is isentropic: the isentropes parallel the surface both along the plateau and the slope. However, as shown by Eliassen (1980) and further explored by Silvers and Schubert (2012), with higher or steeper terrain it is possible for the topography to puncture the lower isentropes. For example, Figure 7 shows the flow obtained for a steeper plateau (top) and a higher plateau (bottom). In both cases the easterly jet is considerably stronger, and the lower isentropes intersect the surface near the top edge of the plateau, indicating that the critical steepness or height, respectively, has been exceeded. Even though the problem has the isentropic lower boundary $\theta_S(\phi) = \theta_B$ specified, in a small region near the top of the slope of the plateau, the inversion of PV has yielded $\sigma = 0$. Thus, θ is no longer a single-valued function of p there, as can be seen by noting that the isentropes for $\theta = 260$, 265, and 270 K coincide along the upper part of the slope.

4.3. Effects of Other Forcing

The results above show that the easterly LLJ surrounding Antarctica can be explained as the balanced flow induced by an isentropic polar plateau, moderated by a low-level PV anomaly due to radiative cooling. However, while the YOTC analyses of Figure 3 show that the Antarctic topography is nearly an isentropic surface, away from the continent the lower boundary is not isentropic, with the surface potential temperature increasing by 25 to 35 K from the edge of the continent to the equator. Note that the larger increase during the cold season is associated with a stronger midlatitude westerly jet through thermal wind balance and with the large increase in the surrounding sea ice during austral winter. In addition, the YOTC analyses show that the pressure along the top surface $\theta_T = 370$ K is not constant, and that the PV is significantly enhanced in the upper-levels over the polar region. Thus, we now investigate the effects of three other forcing terms for this problem, namely, the variations of surface potential temperature θ_S, the top pressure p_T, and an upper-level PV anomaly.

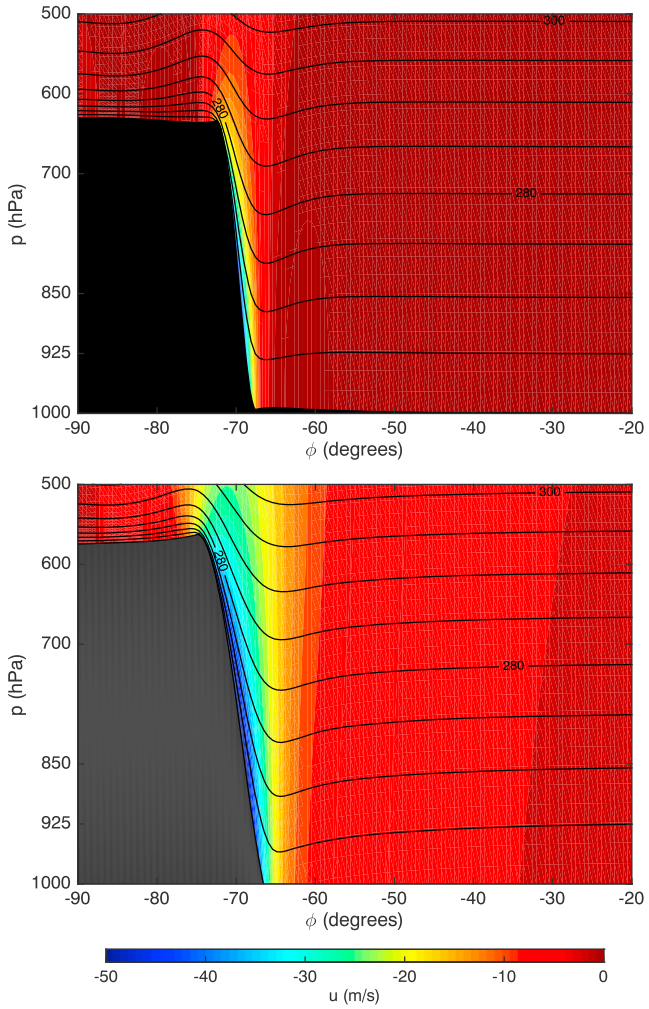

Figure 7. Zonal wind field (shading, 2 m s^{-1} intervals) for isentropic polar plateaus as in Figure 6 but (top) steeper (where $\phi_a = -72.5°$ and $\phi_b = -67.5°$) or (bottom) higher (where $H = 5,000$ m). The maximum easterly winds are 48.6 m s^{-1} and 58.1 m s^{-1}, respectively. Only the lower portion of the domain is shown for clarity.

First, consider the case in which the potential temperature on the lower boundary varies from θ_B at ϕ_c to $\theta_B + \Theta$ at ϕ_d via

$$\theta_S(\phi) = \theta_B + \Theta \begin{cases} 0, & \phi_S \le \phi \le \phi_c, \\ S_\theta\left(\dfrac{\phi - \phi_c}{\phi_d - \phi_c}\right), & \phi_c \le \phi \le \phi_d, \\ 1, & \phi_d \le \phi \le \phi_N, \end{cases} \tag{23}$$

where $S_\theta(s) = 3s^2 - 2s^3 = S_\Phi(1 - s)$ is a cubic Hermite function giving a smooth transition from 0 at $s = 0$ to 1 at $s = 1$. This specification of $\theta_S(\phi)$ is designed to roughly fit the YOTC analysis for the cold season (JJA) shown in Figure 3, with a smooth extrapolation into the south polar region that is actually covered by elevated terrain. For the calculations presented here the values $\phi_c = -70°$, $\phi_d = -20°$, and (unless otherwise specified) $\Theta = 35$ K are used.

Figure 8 shows the balanced flow obtained for this case, both without topography (top) and with the polar plateau (22) and the associated enhanced PV (bottom). It is apparent that the deep baroclinic zone associated with the variation in surface potential temperature accounts for the upper-level westerly flow in the analyses of Figure 3 but has little effect on the easterly LLJ. In this case there is a significant massless layer in the computational domain in (ϕ, θ) space, but the westerly flow within it (not shown) is fictitious, as in the null case above.

Second, consider the case where the top of the domain is no longer assumed to be isobaric. Figure 9 shows the balanced flow for the same cases as in Figure 8 but with top pressure smoothly varying (using cubic Hermite functions) from $p_T = 100$ hPa at $\phi = -80°$ to 155 hPa at $\phi = -50°$ and back to 100 hPa at $\phi = -20°$; this variation approximates that of the cold season (JJA) analysis in Figure 3. The solution is qualitatively similar, but the variation in top pressure has weakened the upper-level westerly jet from 38.0 to 31.0 m s^{-1}.

Finally, consider the case where the PV in the upper atmosphere over the pole is enhanced due to the high static stability in the stratosphere. This we investigate by including an upper-level PV anomaly in the form of a Gaussian function with e-folding width 30° in latitude and 15 K in θ, centered at $\phi = -90°$ and $\theta = \theta_T$, designed to mimic the observed upper-level PV in Figure 3. Figure 10 shows the input PV (bottom row) and resulting solution (top row) for conditions approximating the cold season (left column) and warm season (right column). In the cold (JJA) season, the lower-and upper-level PV anomalies have amplitudes −18.6 and −9.7 PV units (20 times and 2 times the background PV there, respectively), in line with the YOTC data, and the resulting low-level and upper-level jets have maximum winds of 22.6 m s^{-1} and 38.7 m s^{-1}, respectively. In the warm (DJF) season, the lower-and upper-level PV anomalies have amplitudes −11.0 and −21.0 PV units (10 times and 6 times the background PV there, respectively), and the surface potential temperature and top pressure have been changed to vary from 270 K and 200 hPa at the South Pole to 295 K and 100 hPa at the northern boundary, respectively, all in line with the YOTC data. The resulting low-level and upper-level jets have maximum winds of 26.4 m s^{-1} and 38.2 m s^{-1}, respectively. The fact that both seasons have similar low-level jets despite the differences in the PV fields is consistent with both the YOTC analyses of Figure 3 and the modeling study of surface winds by Parish and Cassano (2003).

4.4. Discussion

The reasonable agreement between the modeled winds in Figure 10 (top row) and the observed meridional cross sections in Figure 3 suggests that the essence of the low-level easterly jet over the Eastern Antarctic has been captured by the dynamics of this model. Specifically, Figure 6 shows that the LLJ is explained by the topography and moderated by the low-level PV anomaly due to radiative cooling near the top of the plateau, and Figures 8–10 show that variable surface potential temperature, variable top pressure, and upper-level PV anomalies affect the flow elsewhere but only slightly modify the LLJ. This is as should be expected: since the

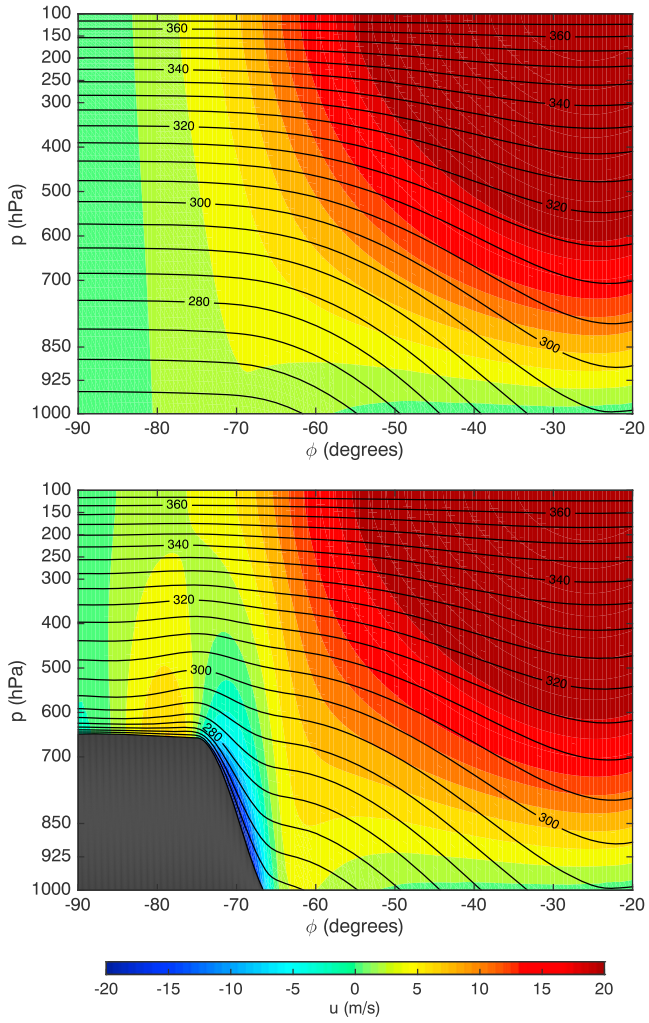

Figure 8. Zonal wind field (shading, 2 m s^{-1} intervals) with surface potential temperature increasing by $\Theta = 35$ K from $\phi_c = -70°$ to $\phi_d = -20°$, both (top) without topography and (bottom) with a polar plateau. Black lines are isentropes with spacing 5 K. The maximum westerly wind is approximately 38 m s^{-1}; in the LLJ (bottom) the maximum easterly wind is 24.4 m s^{-1}.

invertibility relation is an elliptic boundary value problem, its solution at any point depends primarily on the forcing nearby, which for the LLJ means the topography of the plateau and the PV in that region.

Differences between the model solutions and observations can be attributed to a variety of factors, including the following. The fact that the low-level winds (both in the jet and above the plateau) are stronger than the observations may be due to lack of surface friction and free-tropospheric turbulent mixing in the model. Also, the PV fields specified are only idealized approximations to the observed PV (which itself may contain considerable uncertainty, especially in the details above the polar plateau where the vertical resolution is limited). Finally, synoptic-scale features that are not taken into account may affect the flow. In particular, during the JJA period, synoptic-scale pressure gradients, as seen in Figure 2 (left) but not represented in the model, would support easterly flow over the Eastern Antarctic coastal region (Bintanja, 2000). In addition, poleward advection of flow around the eastern flank of the 600 hPa low at 90°E, 70°S would be blocked by the steep terrain in this region, resulting in an easterly barrier flow (O'Connor et al., 1994). The fact that these other features are largely absent during the DJF period (Figure 2, right) yet the low-level easterly jet is still prominent (Figure 3) suggests that the primary explanation of this easterly jet is the PV dynamics of the present model: the jet is the balanced flow associated with the topography and moderated by the effects of radiative cooling. This is consistent with the observation by Parish and Bromwich (2007) that the mean streamlines at 500 m above Antarctica approximately parallel the contour lines of the topography.

5. Dynamical Connections Between Radiative Cooling, Katabatic Winds, and the Easterly Jet

The PV invertibility principle given in (13)–(17) provides a mathematical foundation for understanding the relation of the easterly LLJ with the topography, the potential temperature along the Earth's surface, and the interior PV. However, because the divergent flow components do not appear in the PV invertibility principle, this elliptic invertibility problem does not provide insight into the dynamical connections between katabatic winds and the topographically bound easterly jet. In this section we explore these dynamical connections in a qualitative way, leaving a more thorough quantitative analysis for later work.

Within the context of balanced zonal flow, we can understand these connections through the meridional circulation equation and the potential vorticity equation. We begin by noting that, for the zonally symmetric case, the isentropic coordinate version of the mass continuity equation can be written in the form

$$\frac{\partial(\sigma v \cos\phi)}{a\cos\phi\,\partial\phi} + \frac{\partial(\sigma\dot{\theta} - \partial p/\partial t)}{\partial\theta} = 0, \tag{24}$$

where v is the meridional component of the flow and $\dot{\theta}$ is the diabatic heating.. Equation (24) motivates the representation

$$\sigma v = -\frac{\partial\Psi}{\partial\theta}, \quad \sigma\dot{\theta} - \frac{\partial p}{\partial t} = \frac{\partial(\Psi\cos\phi)}{a\cos\phi\,\partial\phi}, \tag{25}$$

where Ψ is the stream function for the meridional circulation. The zonal momentum equation can then be written in the form

$$\frac{\partial u}{\partial t} + \dot{\theta}\frac{\partial u}{\partial\theta} + \frac{P}{g}\frac{\partial\Psi}{\partial\theta} = F, \tag{26}$$

where F denotes the frictional force per unit mass.

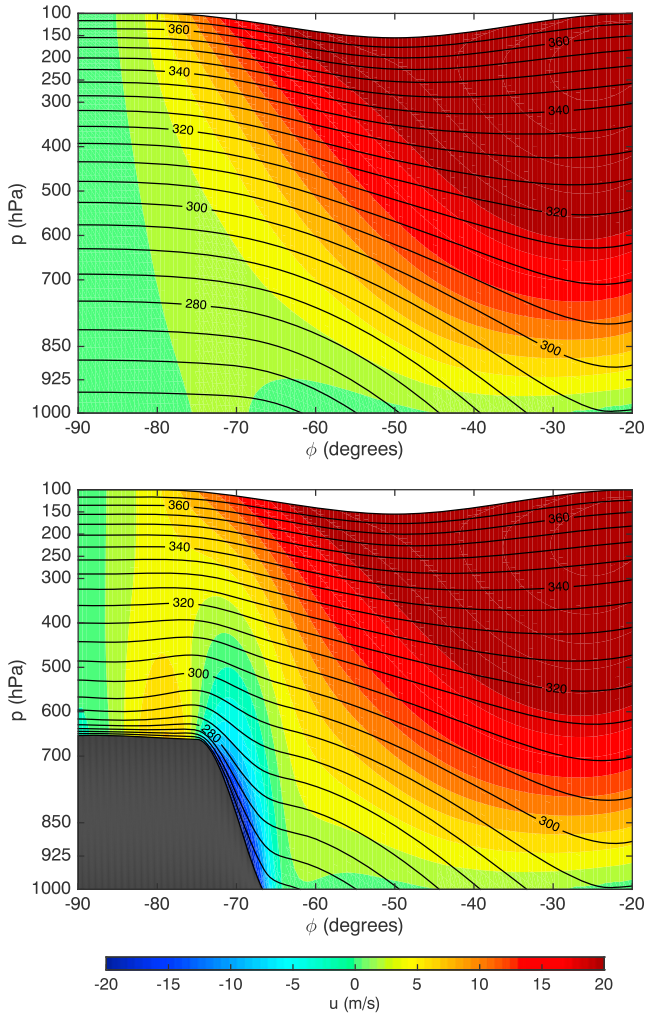

Figure 9. Solution as in Figure 8 except with variable top pressure. The maximum westerly wind is approximately 31 m s^{-1}; in the LLJ (bottom) the maximum easterly wind is 26.7 m s^{-1}.

Taking $\partial^2/\partial\theta\partial t$ of the geostrophic relation $-fu = \partial M/a\partial\phi$ and then making use of the hydrostatic relation $\Pi = \partial M/\partial\theta$, we obtain

$$\frac{\partial}{a\partial\phi}\left(\frac{1}{\rho\theta}\frac{\partial p}{\partial t}\right)+\frac{\partial}{\partial\theta}\left(f\frac{\partial u}{\partial t}\right)=0, \tag{27}$$

which is a constraint on the tendencies of the mass and wind fields such that there be a continuous state of hydrostatic and geostrophic balance. Using the second entry in (25) to eliminate $\partial p/\partial t$ and then using (26) to eliminate $\partial u/\partial t$, we obtain the second-order partial differential equation

$$\frac{\partial}{a\partial\phi}\left(\frac{1}{\rho\theta}\frac{\partial(\Psi\cos\phi)}{a\cos\phi\,\partial\phi}\right)+\frac{\partial}{\partial\theta}\left(\frac{fP}{g}\frac{\partial\Psi}{\partial\theta}\right)=\frac{\partial(\Pi,\dot\theta)}{a\partial(\phi,\theta)}+f\frac{\partial F}{\partial\theta}. \tag{28}$$

A simple interpretation of the first term on the right-hand side of (28) can be obtained by noting that it can be expressed in a more concise mathematical form via the relation

$$\frac{\partial(\Pi,\dot\theta)}{a\partial(\phi,\theta)}=\frac{\partial(\Pi,\dot\theta)}{a\partial(\phi,p)}\frac{\partial(\phi,p)}{\partial(\phi,\theta)}=\frac{\sigma}{\rho\theta}\left(\frac{\partial\dot\theta}{a\partial\phi}\right)_p, \tag{29}$$

where the first equality follows from the Jacobian chain rule, and the second equality from the definition of σ, with the subscript "p" indicating that the ϕ derivative of $\dot\theta$ is taken on an isobaric surface. In other words, the thermal control on the meridional circulation is through the variation of $\dot\theta$ on isobaric surfaces. Equation (28) is elliptic if $fP > 0$, which is always true over the south polar region where $f < 0$ and $P < 0$, and thus, (given appropriate boundary conditions) has a unique solution Ψ. Through (25) and (26) this solution corresponds to that meridional circulation which maintains the wind and mass fields in a continuous state of geostrophic and hydrostatic balance. This circulation is thermally and frictionally controlled by $\dot\theta$ and F and shaped by boundary conditions and by the variable coefficients $(\rho\theta)^{-1}$ and fPg^{-1}.

One useful way of formulating the complete elliptic problem for Ψ is to set F equal to zero and then apply the resulting form of (28) only in the inviscid region above the boundary layer. In this approach the Ball model can be used to obtain the pumping/suction at the top of the boundary layer, that is, to obtain the specified distribution of Ψ along the bottom of the inviscid region. Then, the solution of (28) in the inviscid region determines how the specified boundary layer pumping/suction is extended vertically into the overlying inviscid fluid. Because of the large horizontal extent of Antarctica and because of the large Rossby depth in polar regions, the specified vertical velocity at the top of the boundary layer can extend vertically into the entire troposphere. This is consistent with Parish and Bromwich's (2007) argument that shallow katabatic flows are an important component of the entire mean meridional circulation.

Although the elliptic equation (28) has been formulated in (ϕ,θ) space, the solution $\Psi(\phi,\theta)$ can also be used to compute the vertical p-velocity ω, as can be confirmed by noting that

$$\begin{aligned}\omega&=\frac{\partial p}{\partial t}+v\frac{\partial p}{a\partial\phi}+\dot\theta\frac{\partial p}{\partial\theta}\\&=-\frac{1}{\sigma}\frac{\partial\Psi}{\partial\theta}\left(\frac{\partial p}{a\partial\phi}\right)_\theta-\left(\frac{\partial(\Psi\cos\phi)}{a\cos\phi\,\partial\phi}\right)_\theta\\&=-\left(\frac{\partial(\Psi\cos\phi)}{a\cos\phi\,\partial\phi}\right)_p,\end{aligned} \tag{30}$$

where the first equality follows from the definition of ω, the second equality follows from (25), and the final equality follows from coordinate transformation rules, with the subscript p again indicating that the ϕ derivative is taken on an isobaric surface. To see the structure of the meridional circulation in the YOTC analyses, we have constructed cross sections of the ω field, averaged between 80° and 100°E, for both the cold (JJA)

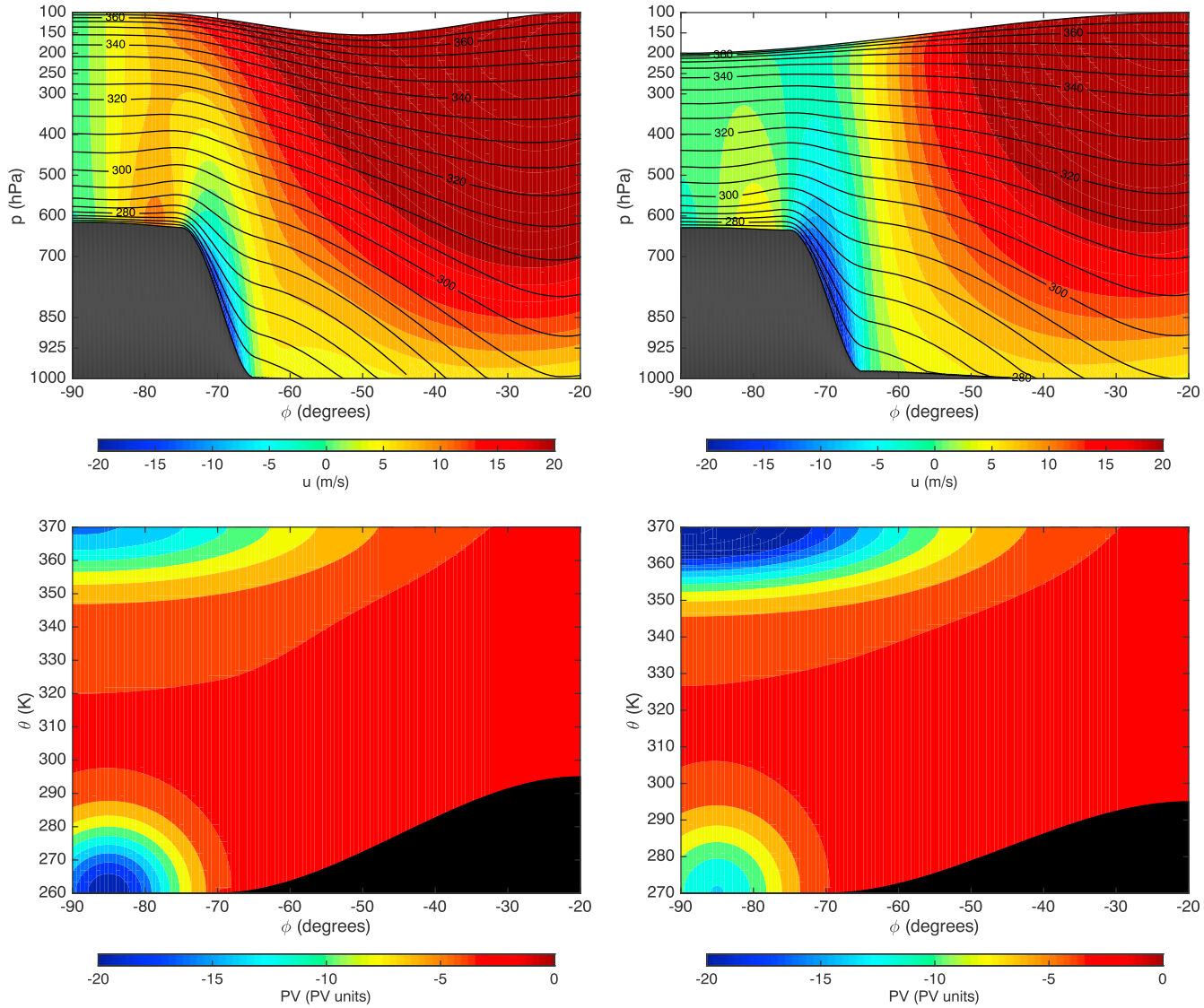

Figure 10. Effects of upper-level PV anomalies. The (top row) solutions are as in Figure 9, based on the (bottom row) specified PV. The left and right columns approximate conditions for the cold (JJA) and warm (DJF) seasons, respectively, with PV values and resulting winds as given in the text.

and warm (DJF) seasons. These cross sections, displayed in Figure 11, reveal large-scale cells with generally weak subsiding motion ($\omega > 0$) in the troposphere and lower stratosphere over the plateau and generally weak rising motion ($\omega < 0$) in the troposphere equatorward of the plateau. Embedded in this large-scale pattern is intense subsidence along the slope, with peak values of 25.5 hPa h^{-1} in JJA and 17.4 hPa h^{-1} in DJF. The resistance to this intense subsidence is weak because, as can be seen in Figure 11, it occurs along surfaces of constant potential temperature. As a measure of the intensity of this seasonal mean katabatic flow, we note that the average time required for parcels to descend along the slope from 600 hPa to 1,000 hPa is approximately 36 h for the cold season (JJA) and 48 h for the warm season (DJF). It is also worth noting that the stronger subsidence values in JJA are consistent with the stronger easterly jet during this period.

Finally, let us consider the role of radiative cooling in producing the negative PV structures just above the Antarctic plateau in Figure 3 (bottom row). The PV equation, derived from the mass continuity equation (24) and the zonal momentum equation (26), can be written in the form

$$\frac{DP}{Dt} = -\frac{g}{\sigma a \cos\phi}\frac{\partial(m,\dot{\theta})}{\partial(\phi,\theta)} - \frac{g}{\sigma}\frac{\partial(F\cos\phi)}{a\cos\phi\,\partial\phi}, \tag{31}$$

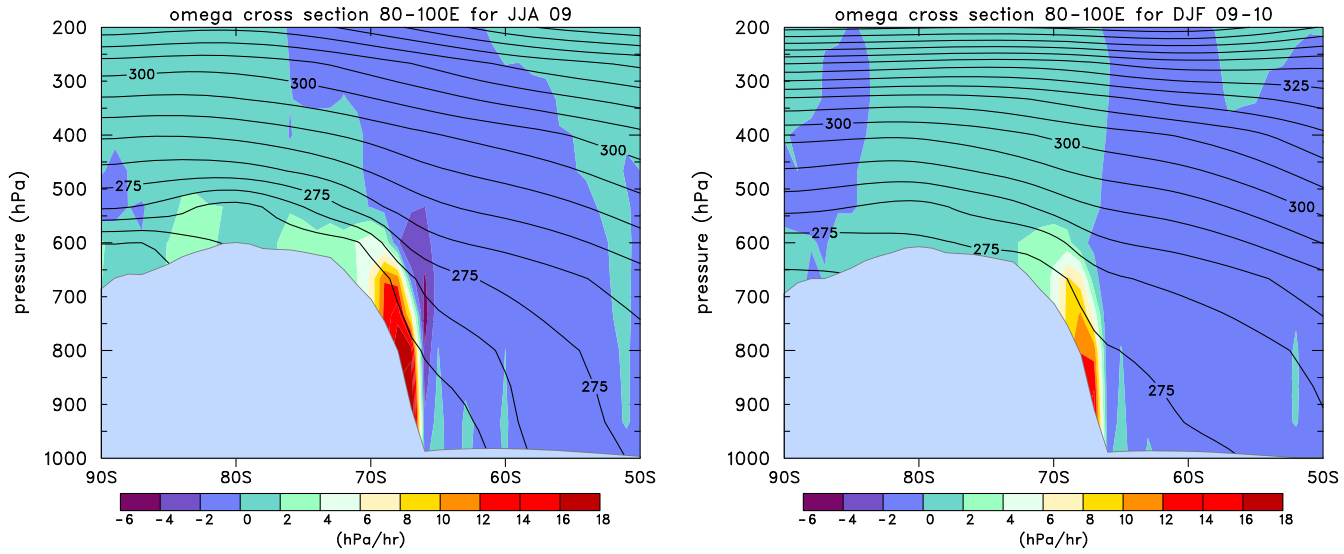

Figure 11. Mean latitude-pressure cross sections of vertical p-velocity ω (shading, interval 2 hPa h^{-1}) and potential temperature θ (contours, interval 5 K) averaged over the longitude sector 80–100°E from the YOTC analyses for the (left) cold season (JJA) and (right) warm season (DJF) as in Figure 3. For clarity, only the region up to 200 hPa and from 90°S to 50°S is shown.

where D/Dt is the total derivative and $m = (u + \Omega a \cos\phi)\cos\phi$ is the absolute angular momentum per unit mass. The first term on the right-hand side of (31) can be expressed in a somewhat simpler form via the relation

$$-\frac{g}{\sigma a \cos\phi}\frac{\partial(m,\dot{\theta})}{\partial(\phi,\theta)} = -\frac{g}{\sigma a \cos\phi}\frac{\partial(m,\dot{\theta})}{\partial(m,\theta)}\frac{\partial(m,\theta)}{\partial(\phi,\theta)} = P\left(\frac{\partial\dot{\theta}}{\partial\theta}\right)_m, \tag{32}$$

where the first equality follows from the Jacobian chain rule, and the second equality from the definition of P, with the subscript "m" indicating that the θ derivative of $\dot{\theta}$ is taken on an absolute angular momentum surface. Using (32) in (31) and for simplicity neglecting frictional effects, we conclude that the PV of a low-level parcel moving toward the edge of Antarctica in a quasi-uniform radiative forcing field behaves as $P(t) = P(0)\exp[(\partial\dot{\theta}/\partial\theta)_m\, t]$, where $P(0)$ is the PV at the beginning of the trajectory. Using typical JJA values over the Antarctic plateau, $\dot{\theta} \approx -11$°C d^{-1} very near the surface at $\theta = 260$ K and $\dot{\theta} \approx -2$°C d^{-1} higher up at $\theta = 275$ K, we obtain $(\partial\dot{\theta}/\partial\theta)_m \approx 0.6\ d^{-1}$, so the e-folding time for PV along the trajectory is approximately 1.7 days. For a parcel with a residence time of several days on the plateau, the PV may experience several e-folding times as it moves to the edge of the continent. This is consistent with the large negative PV (less than −20 PVU for JJA) shown in Figure 3 (bottom row). As we have shown, this negative PV over the plateau is an important part of the specified data for the PV invertibility problem (13)–(17). For the zonally symmetric case, these specified data also include the topography $\Phi_S(\phi)$ and the potential temperature along the topography, $\theta_S(\phi)$. If the interior PV anomaly is not included in the specified data for the invertibility problem, the specified $\Phi_S(\phi)$ and $\theta_S(\phi)$ produce an easterly jet that is too strong. Thus, the role of radiative cooling is to produce a $\theta_S(\phi)$ field that is nearly constant along the continental slope and also a PV anomaly just above the plateau, both of which contribute to the structure and strength of the easterly jet.

6. Concluding Remarks

We have argued that the topographically bound low-level easterly jet along the eastern coastal region of Antarctica is produced by the unique large-scale, ice-dome topography of the continent. Specifically, we have shown (see Figure 6) that this low-level easterly jet can be modeled in a zonally symmetric setting as a balanced flow over an isentropic polar plateau, with the balanced wind and thermal structure in and around the jet being determined primarily by the topography. The enhanced potential vorticity immediately above the polar plateau produced by strong radiative cooling plays an important role in moderating the strength of the jet.

We also have argued that the low-level easterly jet is dynamically connected to the radiatively driven katabatic flows and have shown how the meridional circulation can be understood in terms of an Eliassen-type elliptic

equation with the frictional and katabatic effects concentrated near the lower boundary. This argument connects the balanced flow model presented here with previous studies of katabatic winds based on the model of Ball (1960) and explains how the radiative cooling helps produce a lower boundary that is nearly isentropic and generates the PV anomaly just above the plateau.

It is interesting to note that the dynamical arguments used here for the zonally symmetric aspects of the Antarctic circulation are very similar to those used by Schubert et al. (1991) in modeling the PV dynamics of the Intertropical Convergence Zone and the tropical Hadley circulation. While the fundamental balanced dynamics of these two meridional circulation cells are similar, the forcing processes are quite different, with the tropical Hadley cell forced primarily by deep moist convection and the Antarctic cell forced primarily by topography and shallow radiative processes.

Finally, Parish and Bromwich (2007) have shown that the mean flow at 500 m above ground level tends to follow the contour lines of the complex topography over most of Antarctica (see their Figure 6b); the flow we have identified as the easterly LLJ may be a particularly prominent example associated with the relatively simple topography of the steep, high eastern plateau. In future work we plan to extend our numerical solution of the invertibility principle to three dimensions to study the extent to which PV dynamics can explain the asymmetrical aspects of this topographically bound flow.

Appendix A: Derivation of the Ball Model

The model of Ball (1960) is given by (1) and (2). To solve for V, subtract $(fh/kV)\mathbf{k}\times(1)$ from (1) to obtain

$$\mathbf{u} = \frac{(kV/h)\mathbf{F} - f\mathbf{k}\times\mathbf{F}}{f^2 + (kV/h)^2}. \tag{A1}$$

Strictly speaking, (A1) is not an explicit solution of the nonlinear vector equation (1). It is actually an implicit equation for $\mathbf{u}$ because of the dependence of the wind speed V on the horizontal vector velocity $\mathbf{u}$. However, we can obtain an explicit solution for the wind speed by taking the magnitude of each side of (A1) and then squaring the result. Making use of the relations $\mathbf{F}\cdot(\mathbf{k}\times\mathbf{F}) = 0$ and $(\mathbf{k}\times\mathbf{F})\cdot(\mathbf{k}\times\mathbf{F}) = |\mathbf{F}|^2$, we then obtain

$$V^2 = \frac{|\mathbf{F}|^2}{f^2 + (kV/h)^2}. \tag{A2}$$

After rearrangement, (A2) can be written in the form

$$\left(\frac{V}{V_0}\right)^4 + 2J\left(\frac{V}{V_0}\right)^2 - 1 = 0, \tag{A3}$$

where V_0 and J are defined by

$$V_0 = \left(\frac{h}{k}|\mathbf{F}|\right)^{1/2} \quad \text{and} \quad J = \frac{f^2 h}{2k|\mathbf{F}|}. \tag{A4}$$

Solving (A3) as a quadratic equation for $(V/V_0)^2$ and choosing the physically relevant root yields

$$\frac{V}{V_0} = \left[\left(J^2+1\right)^{1/2} - J\right]^{1/2}. \tag{A5}$$

Defining β as the wind direction angle relative to $\mathbf{F}$, we can write

$$\cos\beta = \frac{\mathbf{F}\cdot\mathbf{u}}{|\mathbf{F}|\,|\mathbf{u}|} = \frac{(k/h)|\mathbf{F}|}{f^2 + (kV/h)^2} = \frac{V^2}{V_0^2}, \tag{A6}$$

where the first equality follows from the definition of the dot product, the second equality follows from the use of (A1), and the third equality follows from the use of (A2) and (A4). Therefore,

$$\beta = \cos^{-1}\left(\frac{V^2}{V_0^2}\right). \tag{A7}$$

To summarize, given J, the normalized wind speed V/V_0 can be calculated from (A5), after which the wind direction can be calculated from (A7).

Appendix B: Numerical Solution

The zonally symmetric version of the problem (13)–(17) is solved numerically using a multigrid method based on a finite difference discretization as follows. To discretize the problem we introduce the grid points $(\phi_j, \theta_k) = (\phi_S + j\Delta\phi, \theta_B + k\Delta\theta)$ with $j = 0, 1, \ldots, m$ and $k = 0, 1, \ldots, n$, where $\Delta\phi = (\phi_N - \phi_S)/m$ and $\Delta\theta = (\theta_T - \theta_B)/n$. We then seek an approximate solution with gridpoint values $\psi_{j,k} \approx \psi(\phi_j, \theta_k)$ satisfying the discrete equation

$$\alpha_{j,k}\left(\frac{a_j\psi_{j-1,k} - d_j\psi_{j,k} + b_j\psi_{j+1,k}}{a^2\Delta\phi^2}\right) + f_j\left(\frac{\psi_{j,k-1} - 2\psi_{j,k} + \psi_{j,k+1}}{\Delta\theta^2}\right) = F_{j,k}, \tag{B1}$$

where $f_j = 2\Omega\sin\phi_j$,

$$\alpha_{j,k} = \begin{cases} \dfrac{g}{\theta_k\rho_{j,k}P_{j,k}}, & \theta_S(\phi_j) < \theta_k < \theta_T, \\ 0, & \theta_B < \theta_k < \theta_S(\phi_j), \end{cases} \tag{B2}$$

and

$$F_{j,k} = \frac{\tilde{\sigma}_k}{\theta_k\tilde{\rho}_k} - \alpha_{j,k}f_j, \tag{B3}$$

with $P_{j,k} = P(\phi_j, \theta_k)$, $\tilde{\sigma}_k = \tilde{\sigma}(\theta_k)$, and $\tilde{\rho}_k = \tilde{\rho}(\theta_k)$. The values $\rho_{j,k}$ are related to the solution values $\psi_{j,k}$ via

$$\rho_{j,k} = \frac{p_0}{R\theta_k}\left(\frac{\Pi_{j,k}}{c_p}\right)^{c_v/R} \tag{B4}$$

and

$$\Pi_{j,k} = \tilde{\Pi}_k + f_j\left(\frac{\psi_{j,k+1} - \psi_{j,k-1}}{2\Delta\theta}\right) \tag{B5}$$

with $\tilde{\Pi}_k = \tilde{\Pi}(\theta_k)$. At the interior points $j = 1, \ldots, m-1$ the discretization of the Laplacian appearing in (B1) is based on (18), giving

$$a_j = \frac{c_{j-1/2}}{c_j}, \quad b_j = \frac{c_{j+1/2}}{c_j}, \quad d_j = a_j + b_j, \tag{B6}$$

where $c_j = \cos\phi_j$ and $c_{j\pm1/2} = \cos\phi_{j\pm1/2}$. At the South Pole $j = 0$ the discretization is based on (19), giving $a_j = b_j = 2$ and $d_j = 4$, where we have introduced the ghost point $j = -1$ with the corresponding value determined by the symmetry condition $\psi_{-1,k} = \psi_{1,k}$. At the north boundary $j = m$ we specify $\psi_{j,k}$ as described in section 3. For the top and bottom boundary conditions we introduce the ghost points $k = -1$ and $k = n+1$ and approximate the vertical boundary conditions (B7) and (B8) using centered differences as

$$f_j\left(\frac{\psi_{j,n+1} - \psi_{j,n-1}}{2\Delta\theta}\right) = \Pi_T(\phi_j) - \tilde{\Pi}_T(\phi_j), \tag{B7}$$

and

$$f_j\left[\psi_{j,0} - \theta_B\left(\frac{\psi_{j,1} - \psi_{j,-1}}{2\Delta\theta}\right)\right] = \Phi_S(\phi_j) \tag{B8}$$

for $j = 0, \ldots, m-1$, where $\Pi_T(\phi_j)$ and $\Phi_S(\phi_j)$ are the specified boundary values. Thus, the interior equation (B1) is applied for $j = 0, \ldots, m-1$ and $k = 0, \ldots, n$.

The discrete system (B1)–(B8) is quasilinear, due to the dependence of ρ—and hence α—on ψ. Since the system is large and sparse, it is best solved by an iterative method. We use a multigrid method, similar to that of Chen and Fulton (2010). On each grid the discrete equation (B1) is relaxed using alternating direction line relaxation, holding the ghost point values fixed during each sweep and then updating them after the sweep via the boundary conditions. This relaxation is embedded in a *V*-cycle control algorithm, with residuals transferred to coarser grids using full weighting and corrections transferred to finer grids using bilinear interpolation. The density ρ is held fixed during each cycle and then updated on the finest grid after the cycle via (B4) and (B5). This method achieves typical multigrid efficiency, that is, residuals are reduced by a factor of about 0.6 per sweep independent of the mesh size. Typically, only three *V*-cycles are needed to achieve sufficient accuracy.

The results presented here were computed using a finest grid with $m \times n = 1,024 \times 512$ grid intervals, giving mesh size 0.068° in latitude (approximately 7.6 km) and 0.21 K in θ. Eight coarser grids were used. Once the stream function is computed, the wind field can be computed from

$$u_{j,k} = -\left(\frac{\psi_{j+1,k} - \psi_{j-1,k}}{2a\Delta\phi}\right) \tag{B9}$$

and the pressure field can be computed from (B5) and the definition of Π.

Acknowledgments
We would like to thank Chris Slocum and Rick Taft for their valuable advice and for assistance with the figures. The reanalysis data used in creating Figures 2, 3, and 11 were provided by the European Centre for Medium-Range Weather Forecasts and were available at http://apps.ecmwf.int/datasets/data/yotc-od/levtype=sfc/type=an/. This research was supported by the National Science Foundation under collaborative grants with award numbers AGS-1147431 and AGS-1601628 to Clarkson University and AGS-1147120 and AGS-1601623 to Colorado State University.

References

Ball, F. K. (1960). *Winds on the ice slopes of Antarctica*. Paper presented at Proceedings of the Symposium on Antarctic Meteorology (pp. 9–16). New York, Melbourne, Australia: Pergamon Press.

Bintanja, R. (2000). Mesoscale meteorological conditions in Dronning Maud Land, Antarctica, during summer: A qualitative analysis of forcing mechanisms. *Journal of Applied Meteorology*, *39*, 2348–2370.

Charney, J. G., & Stern, M. E. (1962). On the stability of internal baroclinic jets in a rotating atmosphere. *Journal of Atmospheric Sciences*, *19*, 159–172.

Chen, Y., & Fulton, S. R. (2010). An adaptive continuation-multigrid method for the balanced vortex model. *Journal of Computational Physics*, *229*, 2236–2248.

Eliassen, A. (1980). Balanced motion of a stratified, rotating fluid induced by bottom topography. *Tellus*, *32*, 537–547.

Fulton, S. R., & Schubert, W. H. (1991). Surface frontogenesis in isentropic coordinates. *Journal of Atmospheric Sciences*, *48*, 2534–2541.

Hoch, S. W., Calanca, P., Philipona, R., & Ohmura, A. (2007). Year-round observation of longwave radiative flux divergence in Greenland. *Journal of Applied Meteorology and Climatology*, *46*, 1469–1479.

Hudson, S. R., & Brandt, R. E. (2005). A look at the surface-based temperature inversion on the Antarctic plateau. *Journal of Climate*, *18*, 1673–1696.

King, J. C., & Turner, J. (1997). *Antarctic meteorology and climatology*. Cambridge Atmospheric and Space Science Series (p. 409). Cambridge, UK: Cambridge University Press.

Kottmeier, C., & Stuckenberg, H.-U. (1986). Quasi-geostrophic flow solution for the circulation over Antarctica. *Beiträge zur Physik der Atmosphäre*, *59*, 491–504.

Kuo, H. L. (1959). Finite amplitude three-dimensional harmonic waves on the spherical Earth. *Journal of Meteorological*, *16*, 524–534.

Mather, K. B. (1969). The pattern of surface wind flow in Antarctica. *Pure and Applied Geophysics*, *75*, 332–354.

Mather, K. B., & Miller, G. S. (1967). Notes on topographic factors affecting the surface wind in Antarctica, with special reference to katabatic winds, and bibliography (Antarctic topographic effects on prevailing surface winds) (*Tech. Rep. No. GA-900*). Fairbanks, Alaska: University of Alaska.

O'Connor, W. P., Bromwich, D. H., & Carrasco, J. F. (1994). Cyclonically forced barrier winds along the Transantarctic Mountains near Ross Island. *Monthly Weather Review*, *122*, 137–150.

Parish, T. R., & Bromwich, D. H. (1987). The surface wind field over the Antarctic ice sheets. *Nature*, *328*, 51–54.

Parish, T. R., & Bromwich, D. H. (2007). Reexamination of the near-surface airflow over the Antarctic continent and implications on atmospheric circulations at high southern latitudes. *Monthly Weather Review*, *135*, 1961–1973.

Parish, T. R., & Cassano, J. J. (2003). The role of katabatic winds on the Antarctic surface wind regime. *Monthly Weather Review*, *131*, 317–333.

Phillpot, H. R., & Zillman, J. W. (1970). The surface temperature inversion over the Antarctic continent. *Journal of Geophysical Research*, *75*, 4161–4169.

Schubert, W. H., Ciesielski, P. E., Stevens, D. E., & Kuo, H.-C. (1991). Potential vorticity modeling of the ITCZ and the Hadley circulation. *Journal of Atmospheric Sciences*, *48*, 1493–1509.

Schubert, W. H., & Masarik, M. T. (2006). Potential vorticity aspects of the MJO. *Dynamics of Atmospheres and Oceans*, *42*, 127–151.

Schubert, W. H., Silvers, L. G., Masarik, M. T., & Gonzalez, A. O. (2009). A filtered model of tropical wave motions. *Journal of Advances in Modeling Earth Systems*, *1*, Art. #3.

Schubert, W. H., Taft, R. K., & Silvers, L. G. (2009). Shallow water quasi-geostrophic theory on the sphere. *Journal of Advances in Modeling Earth Systems*, *1*, 1–17.

Silvers, L. G., & Schubert, W. H. (2012). A theory of topographically bound balanced motions and application to atmospheric low-level jets. *Journal of Atmospheric Sciences*, *69*, 2878–2891.

Smith, R. B. (1979). The influence of mountains on the atmosphere. *Advances in Geophysics*, *21*, 87–230.

Waliser, D. E., Moncrieff, M., Burridge, D., Fink, A. H., Gochis, D., Goswami, B. N., … Yuter, S. (2012). The 'Year' of tropical convection (May 2008 to April 2010): Climate variability and weather highlights. *Bulletin of the American Meteorological Society*, *93*, 1189–1218.

Zwally, H. J., Comiso, J. C., Parkinson, C. L., Campbell, W. J., Carsey, F. D., & Cloersen, D. (1983). Antarctic sea ice, 1973–1976, satellite passive microwave observations (*Tech. Rep.*) Washington, DC: National Aeronautics and Space Administration.